

See discussions, stats, and author profiles for this publication at: <https://www.researchgate.net/publication/330530025>

Memory CD4+ T cells are generated in the human fetal intestine

Article in *Nature Immunology* · January 2019

DOI: 10.1038/s41590-018-0294-9

CITATIONS

2

READS

240

18 authors, including:



Na Li

Leiden University Medical Centre

16 PUBLICATIONS 171 CITATIONS

[SEE PROFILE](#)



Vincent van Unen

Stanford Medicine

47 PUBLICATIONS 126 CITATIONS

[SEE PROFILE](#)



Tamim Abdelaal

Delft University of Technology

6 PUBLICATIONS 2 CITATIONS

[SEE PROFILE](#)



Kristin Ladell

Cardiff University

139 PUBLICATIONS 2,236 CITATIONS

[SEE PROFILE](#)

Some of the authors of this publication are also working on these related projects:



Visual Analysis in Population Imaging Research (VAnPIRe) [View project](#)



3D Active Shape Modeling for Cardiac MRI and CT Image Segmentation [View project](#)

Memory CD4⁺ T cells are generated in the human fetal intestine

Na Li¹, Vincent van Unen¹, Tamim Abdelaal^{2,3}, Nannan Guo¹, Sofya A. Kasatskaya^{4,5}, Kristin Ladell⁶, James E. McLaren⁶, Evgeny S. Egorov⁴, Mark Izraelson⁴, Susana M. Chuva de Sousa Lopes⁷, Thomas Höllt^{2,8}, Olga V Britanova⁴, Jeroen Eggermont⁹, Noel F. C. C. de Miranda¹⁰, Dmitriy M. Chudakov^{4,5,11,12,13,14}, David A. Price¹⁵, Boudewijn P. F. Lelieveldt^{3,9} and Frits Koning^{1*}

The fetus is thought to be protected from exposure to foreign antigens, yet CD45RO⁺ T cells reside in the fetal intestine. Here we combined functional assays with mass cytometry, single-cell RNA sequencing and high-throughput T cell antigen receptor (TCR) sequencing to characterize the CD4⁺ T cell compartment in the human fetal intestine. We identified 22 CD4⁺ T cell clusters, including naive-like, regulatory-like and memory-like subpopulations, which were confirmed and further characterized at the transcriptional level. Memory-like CD4⁺ T cells had high expression of Ki-67, indicative of cell division, and CD5, a surrogate marker of TCR avidity, and produced the cytokines IFN- γ and IL-2. Pathway analysis revealed a differentiation trajectory associated with cellular activation and proinflammatory effector functions, and TCR repertoire analysis indicated clonal expansions, distinct repertoire characteristics and interconnections between subpopulations of memory-like CD4⁺ T cells. Imaging mass cytometry indicated that memory-like CD4⁺ T cells colocalized with antigen-presenting cells. Collectively, these results provide evidence for the generation of memory-like CD4⁺ T cells in the human fetal intestine that is consistent with exposure to foreign antigens.

Adaptive immunity is founded on the selection and expansion of antigen-specific T cells from a clonally diverse pool of naive precursors¹. Naive T cells recirculate among lymph nodes to survey the array of peptide epitopes bound to major histocompatibility complex (MHC) proteins on the surface of antigen-presenting cells (APCs), and functional recognition of a given peptide–MHC molecule is governed by various danger signals and specific engagement via the clonotypically expressed TCR. This triggers a program of differentiation and proliferation that results in the generation of effector T cells, which home to the site of the primary infection and contribute to pathogen clearance, and memory T cells, which remain in the circulation and mediate anamnestic responses to secondary infection. In the last decade, it has also become clear that tissue-resident T cells are commonly present at barrier sites, including the intestine².

Fundamental knowledge of adaptive immunity during early life remains sparse. The infantile intestine is known to harbor clonally expanded T cells³, which have also been identified in the human fetal intestine, but rarely in fetal mesenteric lymph nodes, fetal thymus or fetal spleen, suggesting compartmentalization⁴. In addition, a rare population of CD4⁺ T cells displaying a memory and proinflammatory phenotype has been identified in umbilical cord blood⁵. Although the dogma of a sterile womb has been challenged by reports of bacteria colonization in the placenta^{6,7}, amniotic fluid^{8,9}

and meconium¹⁰, others have questioned these results¹¹. Here we have combined functional studies with mass cytometry, RNA sequencing (RNA-seq) and high-throughput TCR sequencing to perform an in-depth analysis of the fetal intestinal CD4⁺ T cell compartment. Our results provide evidence for memory formation in the human fetal intestine, consistent with in utero exposure to foreign antigens.

Results

Human fetal intestinal CD4⁺ T cells are phenotypically diverse.

To explore the CD4⁺ T cell compartment in the human fetal intestine, we applied a mass cytometry panel comprising 35 antibodies (Supplementary Table 1) that was designed to capture the heterogeneity of the immune system to seven lamina propria samples aged 14–21 gestational weeks¹². After data acquisition, we selected CD45⁺ immune cells (Supplementary Fig. 1a) and mined the dataset via hierarchical stochastic neighbor embedding (HSNE)¹³. At the overview level, HSNE landmarks depicted the general composition of the immune system, with clear separation of the CD4⁺ T cell lineage (Supplementary Fig. 1b). We identified 110,332 CD4⁺ T cells, with an average of 15,761 events per fetal intestine, comprising 47.9 ± 9.6% of all immune cells. We then subjected HSNE-defined CD4⁺ T cells (Supplementary Fig. 1b) to t-distributed stochastic neighbor embedding (t-SNE)¹⁴ in Cytosplore¹⁵ to

¹Department of Immunohematology and Blood Transfusion, Leiden University Medical Center, Leiden, the Netherlands. ²Leiden Computational Biology Center, Leiden University Medical Center, Leiden, the Netherlands. ³Department of Pattern Recognition and Bioinformatics Group, Delft University of Technology, Delft, the Netherlands. ⁴Shemyakin–Ovchinnikov Institute of Bioorganic Chemistry, Russian Academy of Sciences, Moscow, Russia. ⁵Centre for Data-Intensive Biomedicine and Biotechnology, Skolkovo Institute of Science and Technology, Moscow, Russia. ⁶Division of Infection and Immunity, Cardiff University School of Medicine, Cardiff, UK. ⁷Department of Anatomy and Embryology, Leiden University Medical Center, Leiden, the Netherlands. ⁸Computer Graphics and Visualization Group, Delft University of Technology, Delft, the Netherlands. ⁹Department of Radiology, Leiden University Medical Center, Leiden, the Netherlands. ¹⁰Department of Pathology, Leiden University Medical Center, Leiden, the Netherlands. ¹¹Central European Institute of Technology, Masaryk University, Brno, Czech Republic. ¹²Department of Molecular Technologies, Pirogov Russian National Research Medical University, Moscow, Russia. ¹³MiLaboratory LLC, Skolkovo Innovation Centre, Moscow, Russia. ¹⁴Privolzhsky Research Medical University, Nizhny Novgorod, Russia. ¹⁵Systems Immunity Research Institute, Cardiff University School of Medicine, Cardiff, UK. *e-mail: F.Koning@lumc.nl

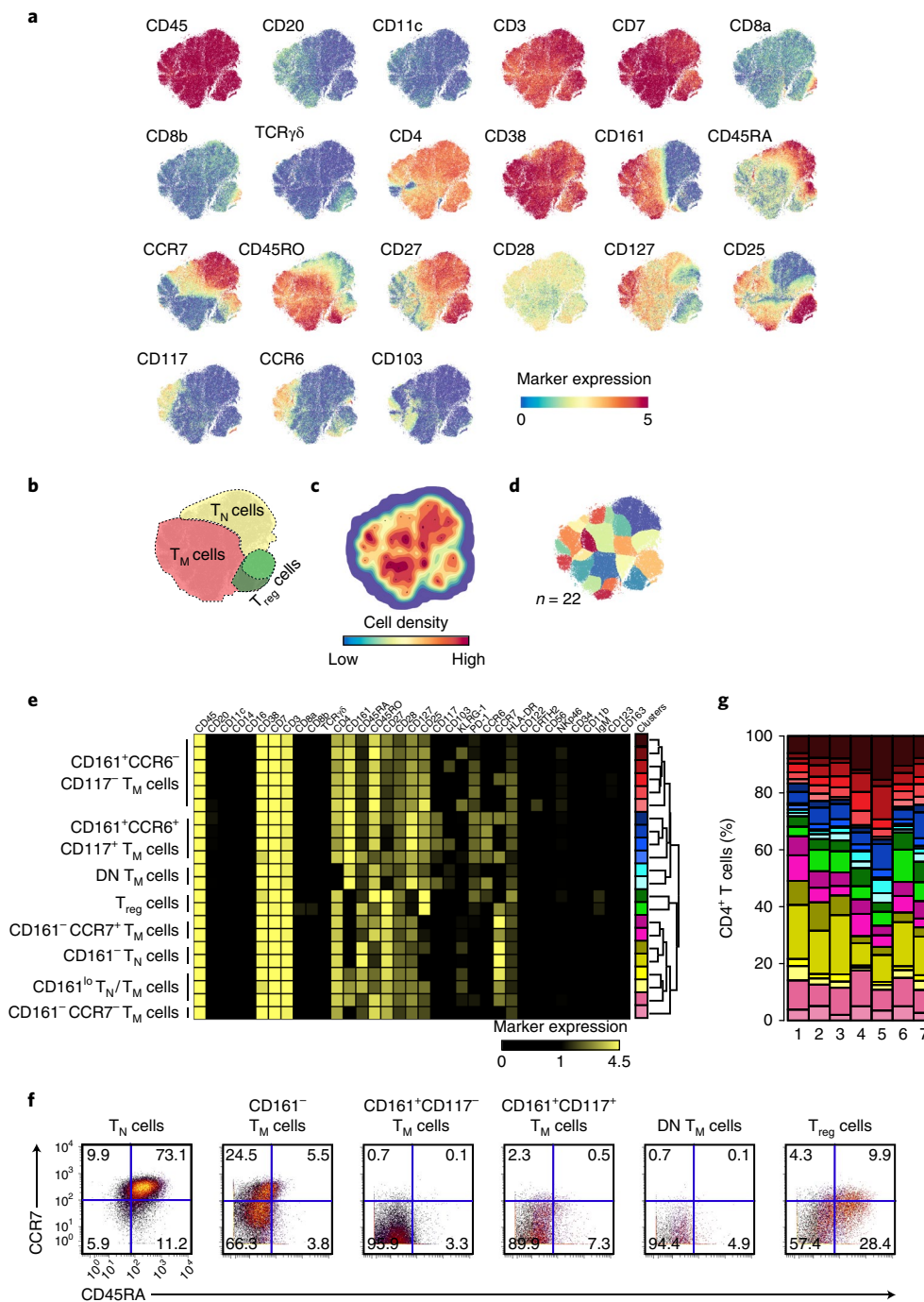


Fig. 1 | Mass cytometric analysis of fetal intestinal CD4⁺ T cells. **a**, t-SNE embedding of all CD4⁺ T cells (n = 110,332) derived from human fetal intestines (n = 7). Colors represent the ArcSinh5-transformed expression values of the indicated markers. **b**, t-SNE plot depicting the population cell border for T_N cells (dashed yellow line), T_M cells (dashed red line) and T_{reg} cells (dashed green line). **c**, Density map describing the local probability density of cells, where black dots indicate the centroids of identified clusters using Gaussian mean-shift clustering. **d**, t-SNE plot showing cluster partitions in different colors. **e**, Heat map showing median expression values and hierarchical clustering of markers for the identified subpopulations. **f**, Biaxial plots showing CD45RA and CCR7 expression on the indicated clusters analyzed by mass cytometry. The 22 clusters were merged into six phenotypic groups according to the heat map shown in **e**. **g**, Composition of the CD4⁺ T cell compartment in each fetal intestine represented by vertical bars, where the colored segment lengths represent the proportion of cells as a percentage of all CD4⁺ T cells in the sample. Colors as shown in **e**.

project their marker expression profiles onto a two-dimensional graph (Fig. 1a and Supplementary Fig. 1c). CD4⁺ T cells were characterized as CD45⁺CD3⁺CD4⁺CD7⁺ (Fig. 1a). Moreover, all CD4⁺ T cells were positive for the tissue-resident marker CD38 and approximately 50% of cells expressed CD161. Of the CD4⁺ T cell population, 24.1% coexpressed CD27, CD28, CD45RA and

CCR7, indicative of a naive T cell (T_N) phenotype, whereas 64.5% expressed CD45RO, indicative of a memory T cell (T_M) phenotype (Fig. 1a,b). While all CD45RO⁺ T_M cells were CD28⁺, differential expression of CD25, CD27, CD103, CD117, CD127, CCR6 and CCR7 was observed on these cells (Fig. 1a,b), reflecting substantial phenotypic diversity.

We next applied Gaussian mean-shift clustering to the mass cytometry data using the t-SNE coordinates of the embedded CD4⁺ T cells (Fig. 1a). On the basis of cell density features (Fig. 1c), this identified 22 distinct CD4⁺ T cell clusters (Fig. 1d), each defined by a unique marker expression profile. Hierarchical clustering of the heat map revealed eight major groups (CD161⁺CCR6⁻CD117⁻ T_M cells, CD161⁺CCR6⁺CD117⁺ T_M cells, double negative (DN) T_M cells, T_{reg} cells, CD161⁻CCR7⁺ T_M cells, CD161⁻ T_N cells, CD161^{lo} T_N/T_M cells and CD161⁻CCR7⁻ T_M cells) (Fig. 1e). High expression of CD25 and a lack of CD127 distinguished two regulatory T cell (T_{reg}) clusters, with either a CD45RA⁺ T_N or a CD45RO⁺ T_M phenotype (Fig. 1a,b,e). The CD161⁺CD4⁺ T cells branched into a CCR6⁻CD117⁻CD45RO⁺ T_M and a CCR6⁺CD117⁺CD45RO⁺ T_M cluster (Fig. 1e). Moreover, CD45RA⁺ T_N and CD45RO⁺ T_M cells were detected in both the CD161⁻ and the CD161^{lo} subpopulations. Additional diversity was observed for the expression of several activation markers, including CRTH2, HLA-DR, KLRG-1 and PD-1, the latter especially within the CD45RO⁺ T_M cell clusters (Supplementary Fig. 1c). Of note, a small population of CD4⁺CD8a⁻TCRγδ⁻ (DN) T_M cells clustered among CD4⁺ T cells in both the HSNE and t-SNE plots. Biaxial plots confirmed coexpression of CD45RA and CCR7 on T_N cells (Fig. 1f), whereas the CD161^{lo}-CD45RO⁺ T_M subpopulation contained both CCR7⁺ central memory T (T_{CM}) cells and CCR7⁻ effector memory T (T_{EM}) cells (Fig. 1f). All other CD45RO⁺ T_M subpopulations harbored primarily T_{EM} cells. Quantification of cellular frequencies for the CD4⁺ T cell clusters per fetal intestine revealed highly similar compositions with all CD45RO⁺ T_M clusters detectable in all samples (Fig. 1g). In contrast, parallel analyses of CD4⁺ T cells isolated from three fetal livers and three fetal spleens, from one shared and two additional fetuses aged 16–21 gestational weeks, revealed a predominance of CD45RA⁺ T_N cells (Supplementary Fig. 2a,b). These results delineated a phenotypically diverse array of human fetal intestinal CD4⁺ T cells, most of which displayed features associated with antigen exposure.

Fetal CD4⁺ T cells display a memory gene expression profile.

We next performed single-cell RNA-seq on flow-sorted fetal intestinal CD4⁺ cells from a lamina propria sample that was also included in the mass cytometry analysis. This yielded data for 1,804 CD4⁺ T cells, identifying cell-specific variable expression of 2,174 genes (see Methods), which were further analyzed using the Seurat computational pipeline¹⁶. Unsupervised clustering revealed nine transcriptionally distinct subpopulations, seven of which corresponded to CD3⁺ T cell subsets, while two displayed a gene expression profile matching CD86⁺HLA-DR⁺ APCs. The corresponding gene expression profiles of the seven T cell subsets were projected onto a single graph using t-SNE (Fig. 2a), and the top 20 upregulated genes were displayed in a heat map (Fig. 2b). Five of the seven RNA-seq-identified CD4⁺ T cell subpopulations corresponded to the mass cytometry-defined CD4⁺ T cell major groups: CCR7⁺ T_N with CD45RA⁺ T_N, KLRB1^{lo}-SELL⁻ T_M with CD161^{lo}-CD45RO⁺ T_M, KLRB1⁺CCR6⁻SELL⁻ T_M with CD161⁺CCR6⁻CD45RO⁺ T_M, KLRB1⁺CCR6⁺SELL⁻ T_M with CD161⁺CCR6⁺CD45RO⁺ T_M and FOXP3⁺ T_{reg} cells with CD25⁺CD127^{lo} T_{reg} cells. The mass cytometry-defined CD161⁻ and CD161^{lo} subpopulations (Fig. 1e) could not be discriminated in the RNA-seq dataset. One additional RNA-seq-identified subpopulation corresponded to proliferating cells, on the basis of the expression of genes associated with cell division (CCNB2, CDK1 and MKI67) (Fig. 2a,b).

As CD45RA and CD45RO were not detectable, we used other markers to distinguish T_M from T_N clusters. To compare gene or marker expression among cell clusters, we used violin plots, displaying the mode average as the thickest section (Fig. 2c–e). Consistent with the mass cytometry data, RNA-seq-defined T_N cells were KLRB1⁻CCR7⁺SELL^{+/−} (Fig. 2c,d), the latter confirmed by flow cytometry (Fig. 2e and Supplementary Fig. 3a). In the absence of

T_M-associated markers, SELL⁻ T_M cell populations were identified on the basis of differential expression of KLRB1 and CCR6 (Fig. 2c,d). Consistent with the mass cytometry data, expression of KIT (CD117) was restricted primarily to KLRB1⁺CCR6⁺SELL⁻ T_M cells (Supplementary Fig. 3b). Moreover, the gene expression profile of the IL2RA⁺IL7R^{lo}FOXP3⁺ T_{reg} cell population (Fig. 2c) corresponded to the mass cytometry-defined CD25⁺CD127^{lo} T_{reg} cells (Fig. 2d). In addition, several RNA transcripts, including LAG3, TIGIT, CTLA4 and TNFRSF18 (or glucocorticoid-induced TNFR-related) ascertained the identity of FOXP3⁺ T_{reg} cells (Fig. 2b). Finally, the RNA-seq data revealed an undefined T_M cluster that was not identified by mass cytometry, but expressed genes similar to those detected in the KLRB1⁺CCR6⁺SELL⁻ T_M subpopulation, such as CD69, CCL5 and JAML. Cell population frequencies identified by mass cytometry and RNA-seq were comparable with the exception of mass cytometry-defined CD25⁺CD127^{lo} T_{reg} cells and RNA-seq-defined FOXP3⁺ T_{reg} cells (Supplementary Fig. 3c).

Compared with the CCR7⁺ T_N population, KLRB1^{lo}-SELL⁻ T_M, KLRB1⁺CCR6⁻SELL⁻ T_M, KLRB1⁺CCR6⁺SELL⁻ T_M and undefined T_M subpopulations had high expression of the tissue-resident and activation-associated gene CD69, the differentiation-promoting gene ANXA1 (Annexin A1), the chemokine-like factor CKLF, the cytokine IL32, the proliferation-associated gene JUN (C-Jun) and the adhesion molecule JAML (Fig. 3a). CD40LG (CD154), TNFSF14 and TGFBI were specifically upregulated by KLRB1⁺CCR6⁻SELL⁻ T_M, KLRB1⁺CCR6⁺SELL⁻ T_M and undefined T_M clusters, while CCL5 and MAP3K8 kinase were upregulated by KLRB1⁺CCR6⁻SELL⁻ T_M and undefined T_M subpopulations. Moreover, IL4I1 was specifically expressed by KLRB1⁺CCR6⁺SELL⁻ T_M and undefined T_M cells. In addition, all fetal SELL⁻ T_M subpopulations had high expression of the tissue-resident genes ITGAE (CD103) and/or CD38 (Fig. 3a).

In agreement with the RNA-seq data, flow cytometry indicated that the activation markers CXCR3, CCR4, CD69 and CD226 were highly expressed on CCR7⁻ T_{EM} cells (Fig. 3b). All CD4⁺ T cells expressed CD95, with the highest expression on CD161⁺ T_{EM} cells (Fig. 3b). Expression of CD31, a marker associated with recent thymic emigrants¹⁷, was highest on CD45RA⁺ T_N cells (Fig. 3b). Thus, RNA-seq confirmed the existence of distinct subpopulations of CD4⁺ T cells and indicated that many genes associated with inflammation and tissue residency were upregulated by fetal CD4⁺ T_M cells, consistent with antigen-driven functionality and maturation.

Computational analysis reveals a differentiation pathway of CD4⁺ T cells.

We next visualized the evolution of the t-SNE computation of the mass cytometry and RNA-seq data to reveal the ordering of single cells along putative differentiation trajectories^{12,15}. At the onset of the mass cytometry data computation, where cells are grouped on the basis of major shared features, CD25⁺CD127^{lo} T_{reg} cells clustered separately from the other cells, whereas the other cell clusters were ordered in a linear fashion with the CD45RA⁺ T_N cells next to the CD161^{lo}-CD45RO⁺ T_M cells, followed by the CD161⁺CCR6⁻CD45RO⁺ T_M cells and the CD161⁺CCR6⁺CD45RO⁺ T_M cells, consecutively (Fig. 4a). A similar phenotypic ordering was observed in parallel analyses of the RNA-seq data, although the KLRB1⁺CCR6⁺SELL⁻ T_M subpopulation aligned differently, but remained connected with the KLRB1⁺CCR6⁻SELL⁻ T_M cluster (Fig. 4b). Individual marker expression patterns at the middle of the t-SNE computation validated the ordering of the clusters and the comparability of the mass cytometry and RNA-seq data (Supplementary Fig. 4a,b). Similar patterns were identified using Diffusion map¹⁸, Vortex¹⁹ and principal component analysis (PCA)²⁰ (Supplementary Fig. 4c–f). Therefore, this analysis reveals a putative differentiation pathway leading to T_M formation.

To extend our analysis of the gene expression profiles underlying this putative differentiation trajectory, we used the pseudotime algorithm in the Monocle toolkit^{21,22}, which calculates the ordering

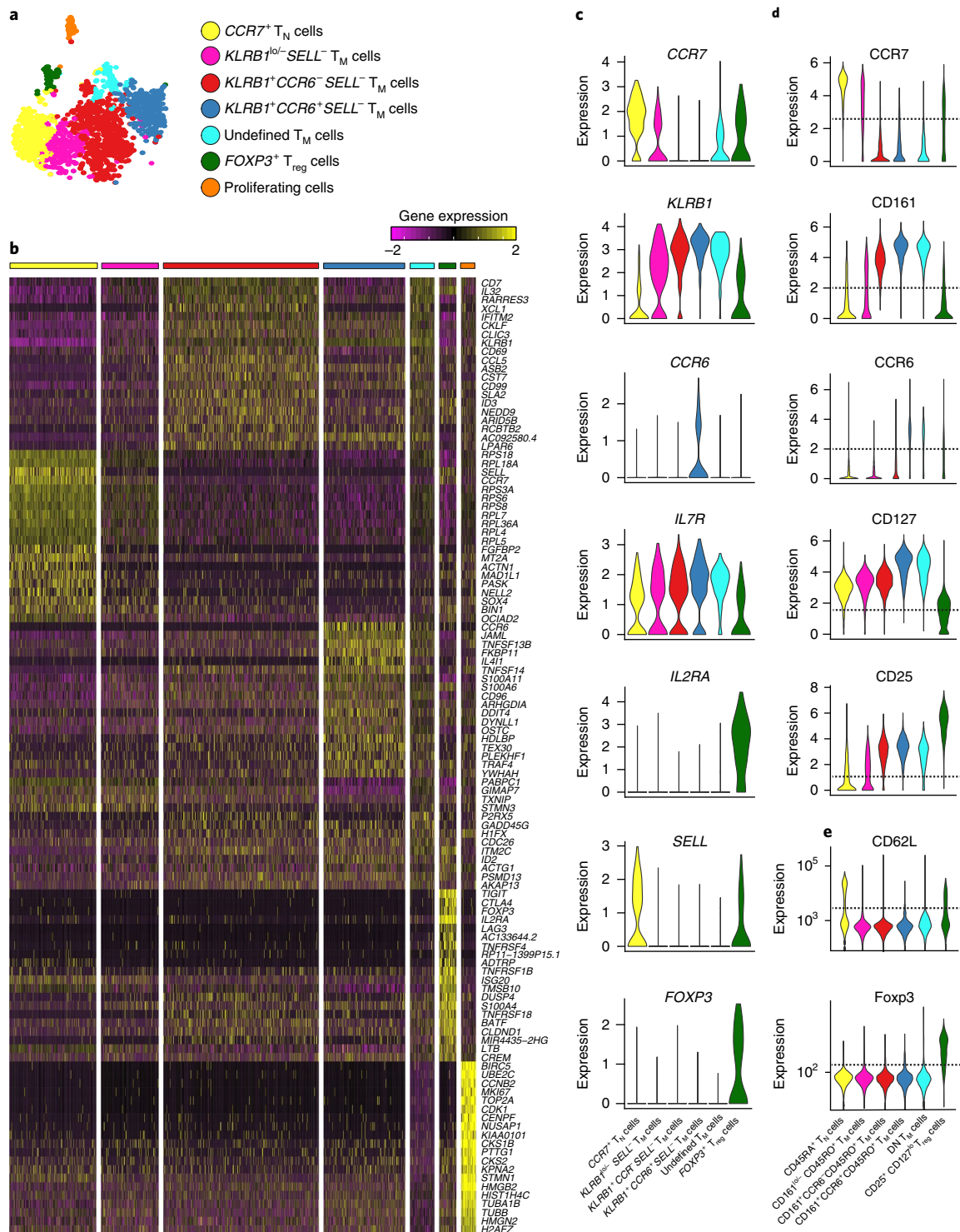


Fig. 2 | Single-cell RNA sequencing of fetal intestinal CD4⁺ T cells. **a**, t-SNE embedding of fetal intestinal CD4⁺ T cells ($n=1,804$) showing seven transcriptionally distinct clusters, including CCR7⁺ T_N cells ($n=358$), KLRB1^{hi}-SELL⁻ T_M cells ($n=237$), KLRB1⁺CCR6⁻SELL⁻ T_M cells ($n=640$), KLRB1⁺CCR6⁺SELL⁻ T_M cells ($n=336$), undefined T_M cells ($n=101$), FOXP3⁺ T_{reg} cells ($n=71$) and proliferating cells ($n=61$). Colors indicate different cell clusters. **b**, Heat map showing the normalized single-cell gene expression value (z score, purple to yellow scale) for the top 20 differentially upregulated genes in each identified cluster. Colors as shown in **a**. **c-e**, Expression of the indicated genes in each identified cluster at the RNA level (log-normalized) (**c**) and the protein level (**d,e**) analyzed by mass cytometry (CyTOF, ArcSinh5-transformed) (**d**) or flow cytometry (**e**), presented as violin plots. Dashed lines indicate background levels. Colors as shown in **a**.

of individual cells on the basis of single-cell expression profiles. On the basis of this analysis, CCR7⁺ T_N cells were separated from SELL⁻ T_M cells (Fig. 4c). When we clustered genes according to expression patterns along the pseudotime trajectory, cell-to-cell transitioning

could be explained by the kinetics of 1,376 variable genes, which formed three large modules (Fig. 4d). The first module contained 540 genes associated with CCR7⁺ T_N cells, including SELL, CCR7, CD27 and CD28 (Fig. 4d). The second module contained 453 genes,

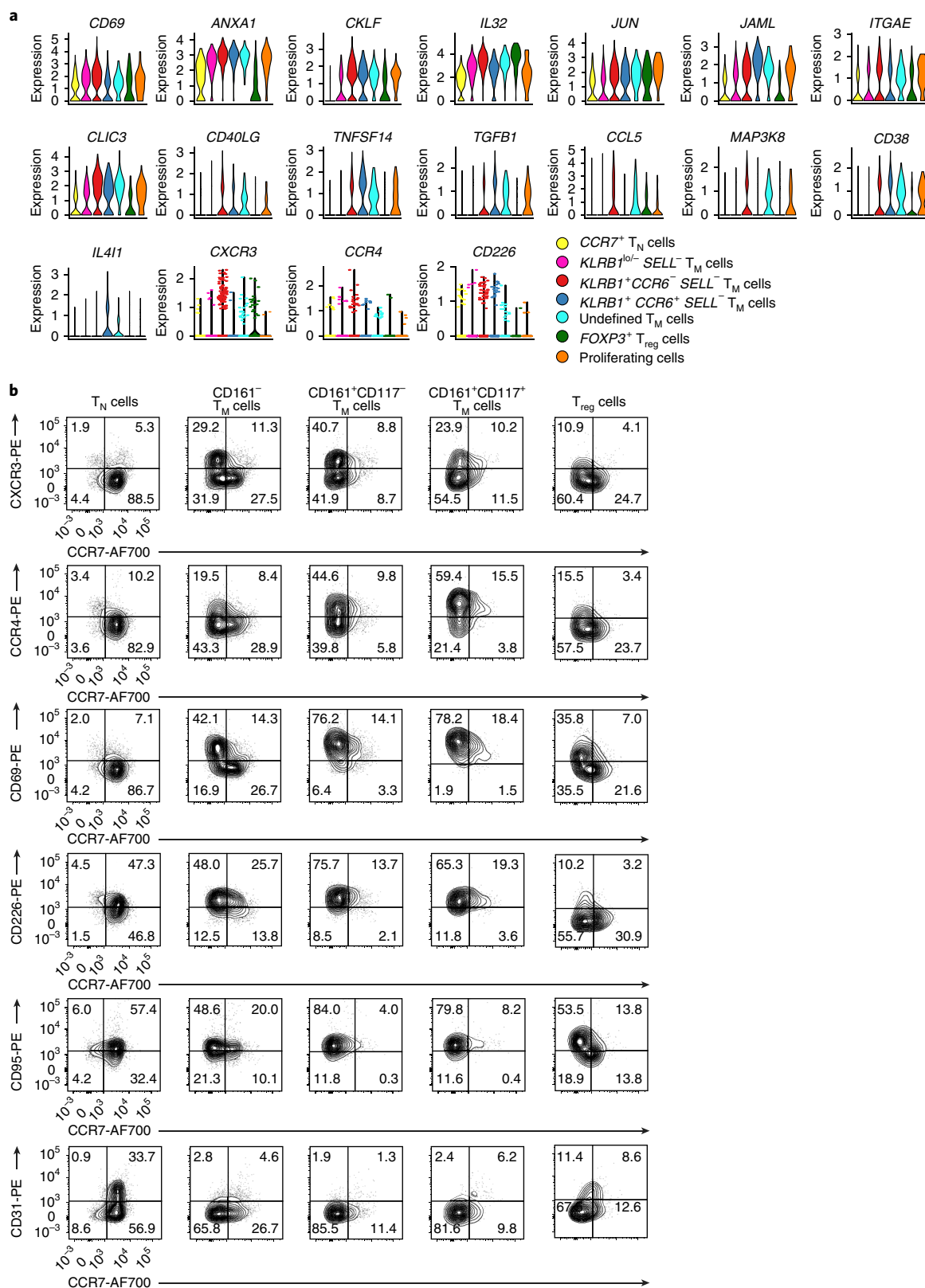


Fig. 3 | Targeted analysis of memory-like fetal intestinal CD4⁺ T cells. **a**, Expression (log-normalized) of the indicated genes in distinct CD4⁺ T cell clusters as determined by single-cell RNA-seq analysis, presented as violin plots. Colors indicate different cell clusters. **b**, Biaxial plots showing expression of CXCR3, CCR4, CD69, CD226, CD95 and CD31 versus CCR7 on the indicated CD4⁺ T cell clusters analyzed by flow cytometry. Data represent two or three independent experiments.

many of which were associated with an ongoing transcriptional program, such as *RPL21*, *RPS2* and *RPLP1*. The highest activity of this transcriptional gene expression profile coincided with the

transition of cells with a *CCR7*⁺ T_N phenotype into cells with a *SELL*⁻ T_M phenotype (Fig. 4c,d). The third module contained 383 genes (Fig. 4d), 106 of which were associated with cellular activation and

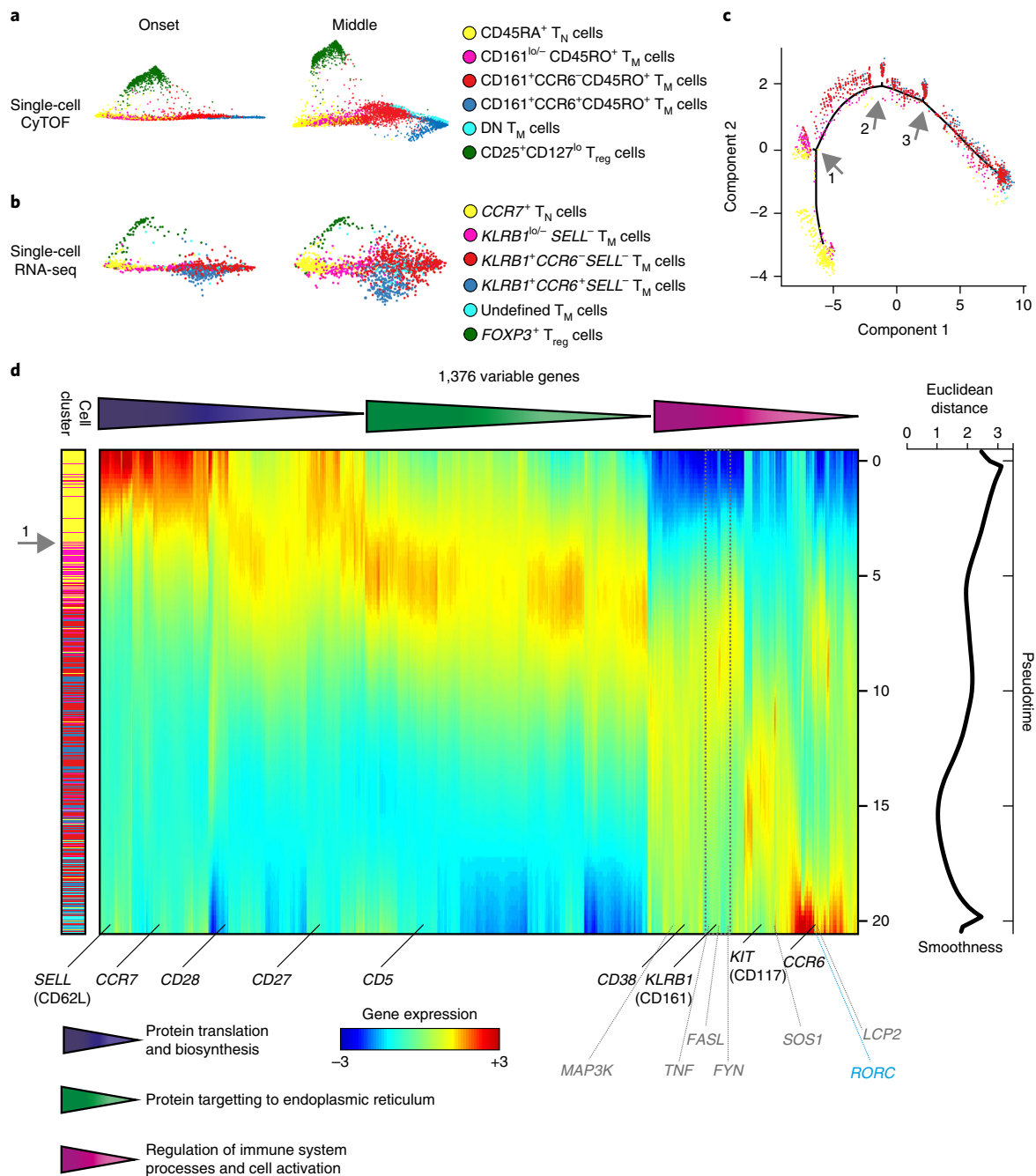


Fig. 4 | Single-cell trajectory analysis of fetal intestinal CD4⁺ T cells. **a, b**, t-SNE embeddings of all fetal intestinal CD4⁺ T cells analyzed by mass cytometry ($n=10,436$) (**a**) and single-cell RNA-seq ($n=1,743$) (**b**) at the onset and at the middle of the t-SNE computation. Colors indicate different cell clusters. **c**, A single-cell trajectory from the RNA-seq data (excluding T_{reg} cells and proliferating cells) recovered by pseudotime analysis. Colors indicate different cell clusters as shown in **b**. Gray arrows indicate three small branches. **d**, Three kinetic modules of pseudotime-dependent genes ($n=1,376$) depicted in a log-variance-stabilized expression heat map, indicating gene-enriched biological processes. Genes confirmed by mass cytometry and flow cytometry are denoted by black labels, and genes involved in TCR signaling are denoted by gray labels. The dashed gray box indicates the coordinated expression profile of *TNF*, *FASL* and *FYN*. Euclidean distance values comparing gene expression profiles for each ordered pair of neighboring cells along the pseudotime trajectory are shown in the graph (right).

regulation of the immune system (Supplementary Fig. 5a), while 133 encoded proteins known to interact physically with each other (Supplementary Fig. 5b). In addition, 23 genes in module 3 could be assigned to cytokine or chemokine receptor pathways, including *CCL20* and its receptor *CCR6*, the interferon receptor *IFNGR1*, TNF family members and IL-1 and IL-17 receptors (Supplementary Fig. 5b). Several signaling cascades were also represented in module 3, including the MAPK, TNF, IL-17 and TCR signaling pathways (*FYN*,

LCP2, *SOS1*, *MAP3K8* kinase, *FASL* and *TNF*) (Fig. 4d). The helper T_H17-associated gene *RORC* was expressed in module 3 (Fig. 4d). In addition, the dynamic expression profiles of *FYN*, *FASL* and *TNF* clustered tightly with *KLRB1* (CD161) (Fig. 4d) at the point in the pseudotime trajectory where CCR7⁺ T_N cells were aligned next to SELL⁻ T_M cells (Fig. 4d). Finally, we quantified the smoothness of cell-to-cell transitioning on the basis of gene expression changes along the trajectory, which showed that the pseudotime trajectory

was most uncertain at the beginning and toward the end, but quite robust in the middle, where $CCR7^+$ T_N cells were aligned next to $SELL^-$ T_M cells (Fig. 4d). In total, these results identified temporal patterns of gene expression along the single-cell trajectory that are compatible with the transition of cells displaying a T_N phenotype into cells with a T_M phenotype.

TCR analysis reveals clonal expansion of fetal $CD4^+$ T cells. Surface expression of CD5 correlates with TCR avidity^{23–26}. Because CD5 gene expression was upregulated in T_M cells compared with T_N cells, we quantified CD5 expression on all identified fetal intestinal $CD4^+$ T cell subsets using flow cytometry. We observed that all the $CD4^+$ T cell subsets expressed CD5 (Fig. 5a), but that the median fluorescence intensity was higher in $CD161^- T_M$, $CD161^+CD117^- T_M$ and $CD161^+CD117^+ T_M$ cells and lower in $CD25^+CD127^{lo} T_{reg}$ cells and $CD45RA^+ T_N$ cells (Fig. 5a–c), suggesting that cells with a T_M phenotype express TCR with a higher avidity compared with T_N cells.

Next, we evaluated the TCR clonotypic architecture of flow-sorted fetal intestinal $CD45RA^+ T_N$, $CD45RO^+ T_M$ and $CD25^+CD127^{lo} T_{reg}$ subpopulations. Analysis of the TCR β rearrangements in a single fetal intestine indicated limited overlap among the distinct subpopulations, most of which were highly polyclonal (data not shown). Distinct clonotypes were expanded among $CD45RO^+ T_M$ cells compared with $CD45RA^+ T_N$ cells (Supplementary Fig. 6a). We then used a quantitative high-throughput approach for deep sequencing of TCR α and TCR β rearrangements in all identified fetal intestinal $CD4^+$ T cell subsets isolated from two additional fetal intestines (Supplementary Table 2). Post-analysis of the repertoires obtained was conducted using VDJtools²⁷. As expected, all T_M subpopulations showed greater clonality compared with the T_N subpopulation (Fig. 5d,e). The averaged characteristics of CDR3 length, added N nucleotides and physicochemical characteristics of the five amino acid residues located in the middle of the CDR3 loop, which are most likely to contact the peptide–MHC complex²⁸, also differed among all subpopulations (Fig. 5f). The latter analysis included the averaged statistical potential of the CDR3 loop with respect to epitope interactions, comprising the estimated ‘energy’ of the interaction with a random epitope²⁹, the ‘strength’ of the interaction (derivative of ‘energy’, VDJtools²⁷), hydrophobicity (Kidera factor 4)^{30,31} and ‘volume’ (values from http://www.imgt.org/IMGTeducation/Aide-memoire/_UK/aminoacids/IMGTclasses.html). These analyses provided no evidence for clonal expansion of $CD4^+$ T cells as a function of intrinsically high TCR avidities for self-derived peptide–MHC complexes (Fig. 5d–f), suggesting indirectly that antigen-specific interactions triggered clonal selection of $CD4^+$ T cells from the T_N cell pool. Analysis of V–J segment use (Jensen–Shannon divergence; Supplementary Fig. 6b) and overlaps among repertoires in terms of the weighted proportion of shared TCR β clonotypes revealed tightly clustered technical replicates and clearly distinguished all subpopulations of $CD4^+$ T cells (Fig. 5g). At the same time, the $CD161^- T_M$, $CD161^+CD117^- T_M$ and $CD161^+CD117^+ T_M$ cells clustered similarly in each fetus, with minimum overlap with the $CD45RA^+ T_N$ and $CD25^+CD127^{lo} T_{reg}$ cells (Fig. 5g). Analysis of the clonal overlap of amino acid CDR3 repertoires between the same populations in the two fetal intestines revealed that the $CD161^- T_M$, $CD161^+CD117^- T_M$ and $CD161^+CD117^+ T_M$ populations displayed much stronger overlap than the $CD45RA^+ T_N$ and $CD25^+CD127^{lo} T_{reg}$ $CD4^+$ T cells (Supplementary Fig. 6c), which could be explained by TCR selection due to exposure to similar foreign antigens. Finally, although the majority of the TCR repertoire was specific for each population, up to 20% of the T cell clones were shared between the $CD45RA^+ T_N$ and the three $CD45RO^+ T_M$ cell populations (Supplementary Fig. 6d), suggesting a potential clonal relationship between $CD45RA^+ T_N$ and $CD45RO^+ T_M$ cells. These results indicate that avidity-based, clonotype-specific expansion of the T_N pool was associated with

T_M formation and confirmed the close relationship between $CD161^- T_M$, $CD161^+CD117^- T_M$ and $CD161^+CD117^+ T_M$ cells.

Fetal $CD4^+$ T_M cells secrete proinflammatory cytokines. To determine the functional profiles of fetal intestinal $CD4^+$ T cells, we flow-sorted $CD3^+CD4^+$ T cells and measured expression of TNF, IL-2, IFN- γ , IL-4, granzyme B and IL-17A in $CD45RA^+ T_N$ cells and $CD117^-$ and $CD117^+ T_M$ cells after cross-linking CD3 and CD28. The activation marker CD154 (CD40L) was upregulated on all cells analyzed (Fig. 6a,b), indicating efficient stimulation. All three subpopulations secreted large amounts of TNF (Fig. 6a,b), but $CD117^- T_M$ cells and $CD117^+ T_M$ cells displayed the highest median fluorescence intensities (Supplementary Fig. 7a). Moreover, IL-2, IFN- γ , IL-4 and granzyme B were more commonly expressed in $CD117^- T_M$ and $CD117^+ T_M$ cells relative to $CD45RA^+ T_N$ cells (Fig. 6a,b). The majority of cytokine-producing $CD4^+$ T cells did not express Ki-67 (Supplementary Fig. 7b). Importantly, higher frequencies of IL-2⁺IFN- γ ⁺ cells were detected in the $CD117^- T_M$ and $CD117^+ T_M$ cells compared with the $CD45RA^+ T_N$ population (Supplementary Fig. 7c), suggesting greater polyfunctionality. Although the T_H17 -associated *RORC* gene was expressed by 1.3% of $KLRB1^+CCR6^+SELL^- T_M$ cells (Fig. 4d), IL-17A production was undetectable in all T_M cells. Thus, fetal intestinal $CD117^- T_M$ and $CD117^+ T_M$ cells deployed multiple effector functions reminiscent of classical $CD4^+$ T_M cells in response to TCR-mediated signal transduction and costimulation via CD28.

Fetal $CD4^+$ T cells are colocalized with antigen-presenting cells.

The single-cell RNA-seq analysis revealed a *MKI67*⁺ cluster of proliferating cells, together with high expression of the T_M cell-associated markers *KLRB1* (CD161) and *CD69* and low expression of the T_N cell-associated markers *CCR7* and *SELL* (CD62L) (Fig. 7a). Flow cytometry of fetal intestinal $CD4^+$ T cells indicated the presence of Ki-67⁺ cells, predominantly within the $CD45RO^+$ compartment (Fig. 7b). To assess the spatial distribution of $CD4^+$ T cells in situ, we employed a panel of 15 antibodies (Supplementary Table 3) combined with a DNA stain to perform imaging mass cytometry on tissue sections of four human fetal intestinal samples. Stains for collagen I and smooth muscle actin were used to visualize the extracellular matrix of the basement membrane, and the epithelium and lamina propria were distinguished as vimentin⁺E-cadherin⁺ and vimentin⁺E-cadherin⁻, respectively (Fig. 7c,d). Most $CD4^+$ T cells localized to the lamina propria (Fig. 7c,d). Differential expression of CD45RA further allowed discrimination of $CD45RA^+ T_N$ (Fig. 7c,d) from $CD45RA^- T_M$ cells in the lamina propria (Fig. 7c,d). In addition, all $CD4^+$ T cells expressed CD38, whereas only some $CD4^+$ T cells expressed CD69 (Fig. 7d). Using a second panel comprising ten antibodies (Supplementary Table 3), we found that $CD4^+$ T cells frequently colocalized with $CD163^+HLA-DR^+$ APCs (Fig. 7e). Moreover, the single-cell RNA-seq analysis of fetal intestinal cells revealed two clusters of cells displaying high expression of gene transcripts encoding HLA-DR, CD74 (HLA-class II invariant chain), inhibitory molecule PD-L1 (CD274), CD80 and CD86, typically found in APCs. Moreover, these APCs expressed gene transcripts encoding CD40, consistent with an activated phenotype (Fig. 7f), whereas stimulated fetal intestinal $CD4^+$ T cells expressed CD40L (CD154) (Fig. 6b). In addition, 25.8% of APCs had high expression of *CCR7*, potentially enabling migration to the mesenteric lymph nodes (Fig. 7f). Collectively, these results indicated the existence of $CD4^+$ T_M cells in the fetal intestine, many of which colocalized in the lamina propria with activated $CD163^+HLA-DR^+$ APCs.

Discussion

Here we used mass cytometry and single-cell RNA-seq to characterize $CD4^+$ T cells in the human fetal intestine. Mass cytometry revealed three major populations of fetal intestinal $CD4^+$ T cells

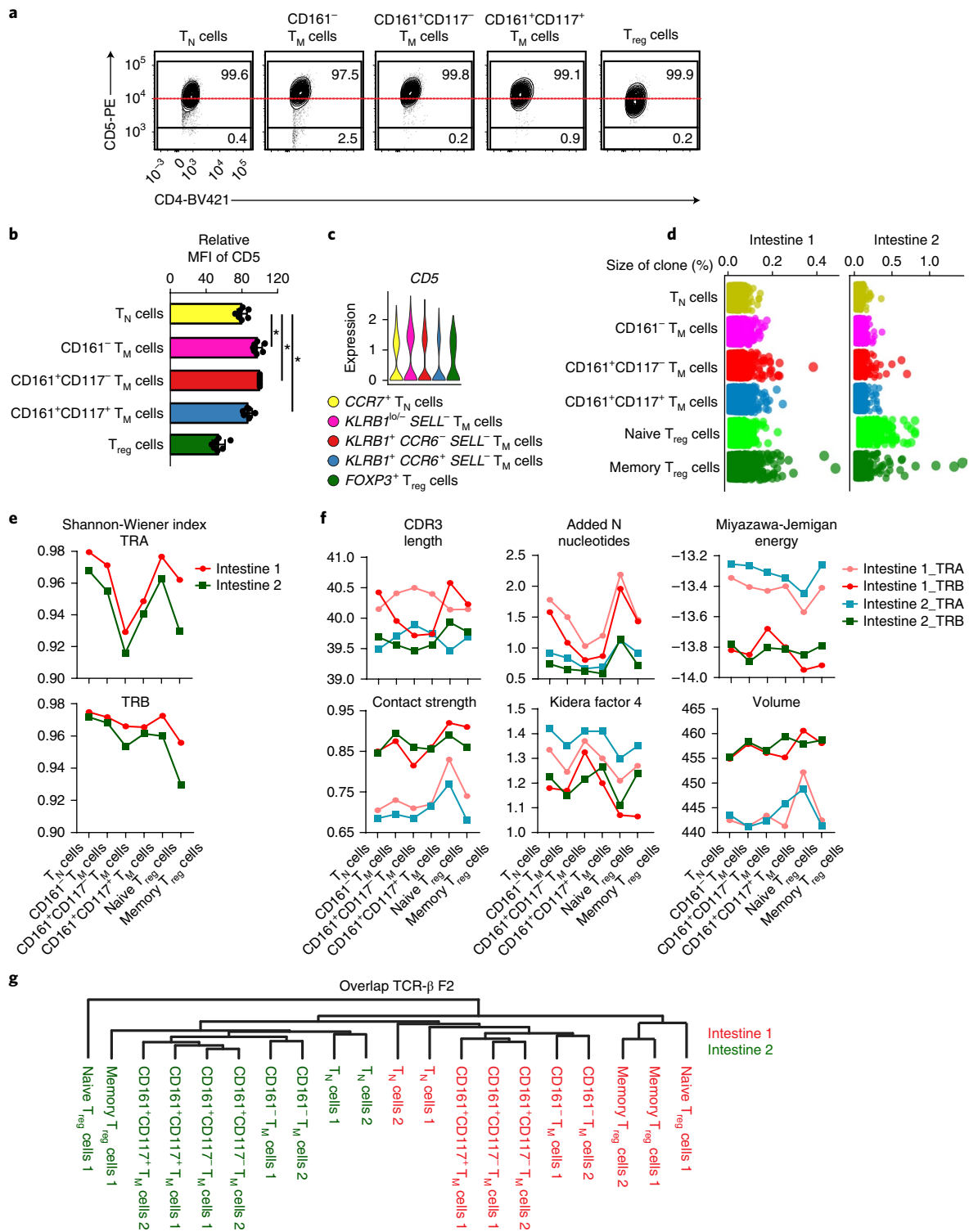


Fig. 5 | CD5 expression analysis and high-throughput TCR sequencing of fetal intestinal CD4⁺ T cells. **a, b**, CD5 expression on the indicated CD4⁺ T cell clusters. The biaxial plots depict one representative experiment (**a**), and the bar graphs depict the median fluorescence intensity (MFI) of CD5 expression for each cluster relative to the corresponding CD161⁺CD117⁻ T_M subpopulation in each fetal intestine ($n=7$) (**b**). Data represent six independent experiments. Error bars indicate mean \pm s.e.m. * $P < 0.05$, two-tailed Wilcoxon matched-pairs signed-ranks test. **c**, Expression (log-normalized) of *CD5* gene transcripts in the indicated cell clusters, presented as violin plots. **d**, Dot plots showing the percentage of TCR cDNA molecules per unique TCR β sequence in each cluster from each fetal intestine. Data are from two independent samples. A single duplicate is shown for samples with technical replicates. **e**, Dot plots showing the normalized Shannon-Wiener index for TCR α (TRA) and TCR β (TRB) sequences in each cluster from each fetal intestine. Data are from two independent samples. **f**, Dot plots showing averaged TCR repertoire characteristics weighted per clonotype for each cluster. Data are from two independent samples. **g**, Dendrogram showing weighted clonal overlaps for TCR β nucleotide sequences among clusters, analyzed using the F2 similarity metric in VDJtools. Colors indicate different fetal intestines.

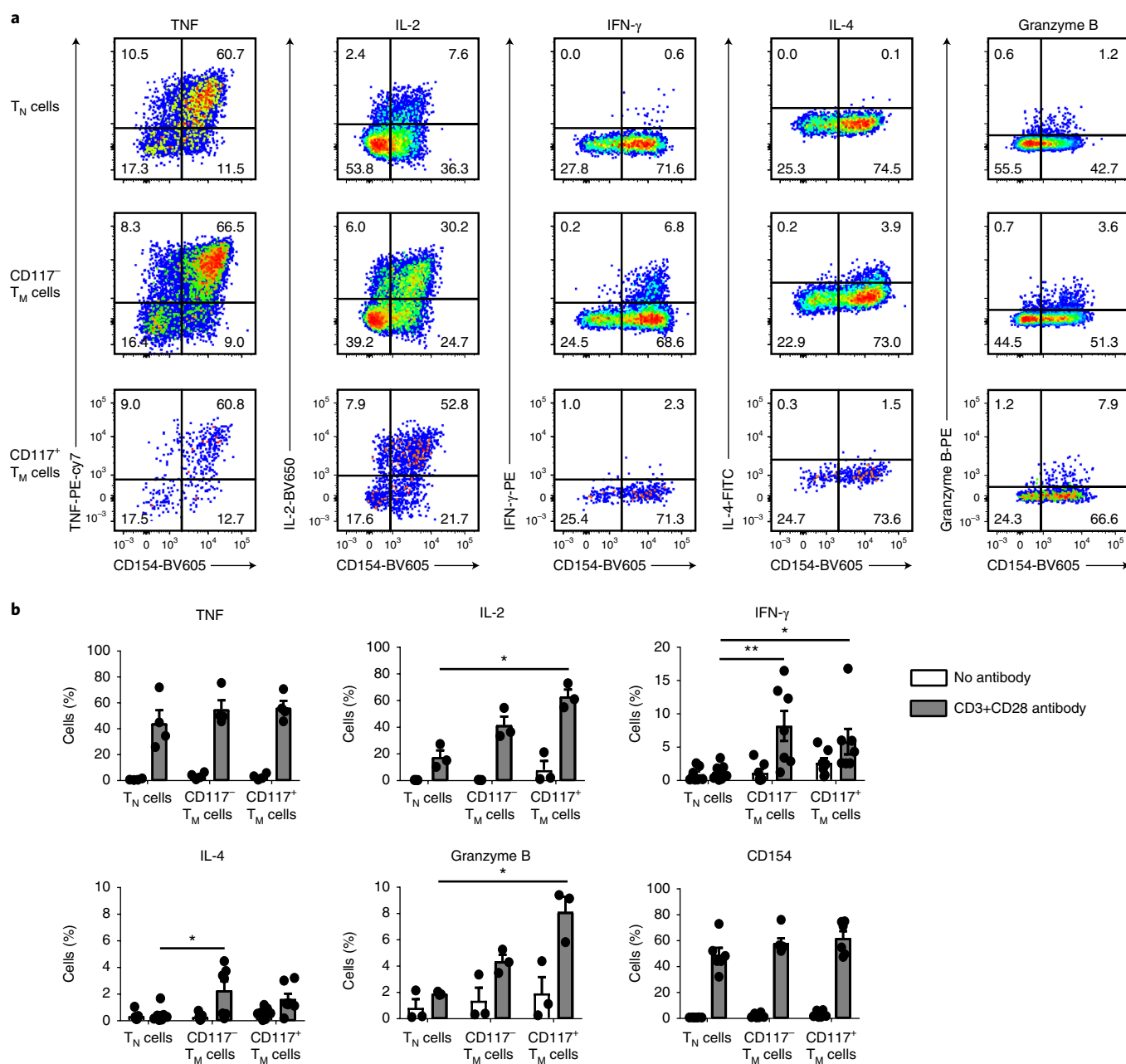


Fig. 6 | Functional profiling of fetal intestinal CD4⁺ T cells. **a, b**, Purified fetal intestinal CD4⁺ T cells were treated with a control antibody or stimulated with anti-CD3 and anti-CD28 for 4 hours. Intracellular expression of TNF, IL-2, IFN- γ , IL-4, granzyme B and CD154 was determined for each subpopulation by flow cytometry. The biaxial plots show data from one representative experiment after stimulation with anti-CD3 and anti-CD28 (**a**) and the bar charts show data for each subpopulation from each fetal intestine (**b**) (TNF: $n=4$ samples in two independent experiments; IL-2 and granzyme B: $n=3$ samples in two independent experiments; IFN- γ , IL-4 and CD154: $n=7$ samples in four independent experiments). Error bars indicate mean \pm s.e.m. * $P < 0.05$, ** $P < 0.01$, Kruskal-Wallis test with Dunn's test for multiple comparisons.

(T_N, T_M and T_{reg} cells), that could be further distinguished into eight distinct cell clusters that displayed additional heterogeneity. These cell clusters were present in seven human fetal intestines, suggesting a physiologically robust immune composition. Single-cell RNA-seq revealed the presence of seven CD4⁺ T cell subpopulations, five of which displayed phenotypic overlap with the mass cytometry-defined CD4⁺ T cell subpopulations. We used computational tools to construct putative CD4⁺ T cell differentiation trajectories. Using adapted t-SNE³², we obtained remarkably similar trajectories for the mass cytometry and RNA-seq data. We identified three distinct gene expression modules along the differentiation trajectory that corresponded to an increase in gene translation and

subsequent activation of immune-related genes. In addition, high-throughput TCR sequencing indicated clonal expansions within the CD4⁺ T_M cell pool, consistent with the evidence for cell proliferation within the CD45RO⁺ T_M pool that was obtained at both the messenger RNA and protein level. Moreover, CD4⁺ T_M cells secreted higher amounts of proinflammatory cytokines on TCR triggering compared with CD4⁺ T_N cells. Finally, fetal intestinal CD4⁺ T_M cells displayed a tissue-resident profile and were frequently found to colocalize with APCs in the lamina propria. Together, this suggests that clonotype-specific transcriptional programs regulated by antigen encounter underpinned the formation of CD4⁺ T_M cells in the fetal intestine.

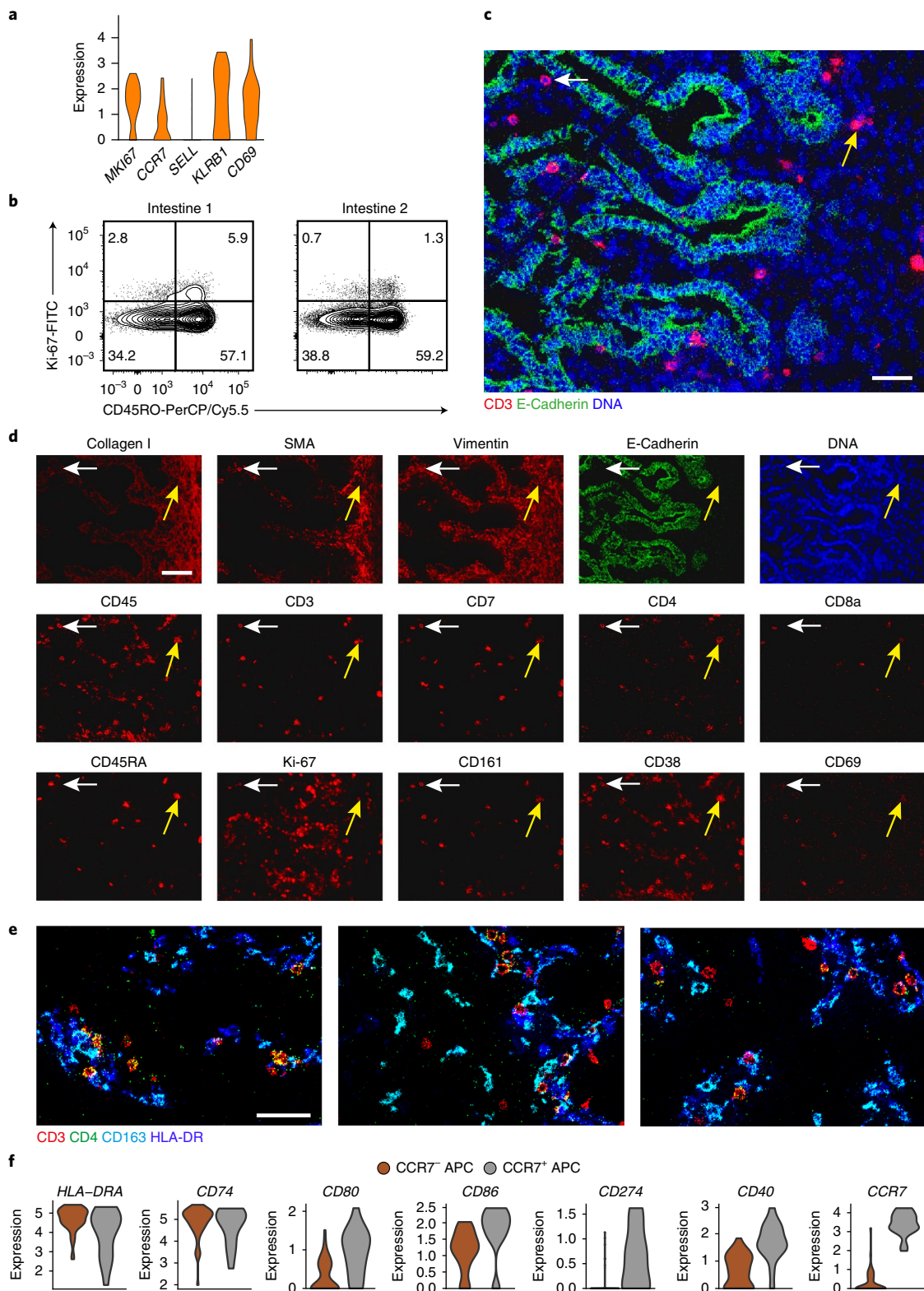


Fig. 7 | Characterization and spatial localization of fetal intestinal CD4⁺ T cells and APCs. **a**, Expression (log-normalized) of the indicated genes in proliferating fetal intestinal CD4⁺ T cells, presented as violin plot. **b**, Biaxial plots showing expression of Ki-67 versus CD45RO in the fetal intestinal CD4⁺ T cell compartment analyzed by flow cytometry. Data represent two independent experiments. **c**, Representative mass cytometry image of a fetal intestine showing the overlay of CD3 (red), E-cadherin (green) and DNA (blue). Scale bar, 100 μ m. **d**, Representative mass cytometry images of fetal intestines showing expression of the indicated stromal markers, immune markers, Ki-67 and DNA by the cells identified in **c**. Scale bar, 200 μ m (applies similarly to all the images in **d**). Yellow arrows: CD4⁺CD45RA⁺ T_N cells; white arrows: CD4⁺CD45RA⁻ T_M cells. **e**, Representative mass cytometry images of a fetal intestine showing the overlay of CD3 (red), CD4 (green), CD163 (cyan) and HLA-DR (blue). Scale bar, 50 μ m. Colors and scale bars are similar in all three panels. Data in **b–d** represent four independent samples in four independent experiments. **f**, Expression (log-normalized) of the indicated genes in two clusters of APCs, presented as violin plots. CCR7⁻ APCs ($n=49$), CCR7⁺ APCs ($n=17$).

T cells in umbilical cord and peripheral blood obtained from infants aged 2 months were reported to display a typical CD45RA⁺T_N phenotype³. The observation herein that a large pool of CD45RO⁺ cells with a tissue-resident profile populated the fetal intestine suggests the compartmentalization of the immune system early in life. In conjunction with the earlier finding that clonally expanded T cells were present in the fetal intestine, but virtually absent in other fetal organs⁴, our results further suggest that memory formation was driven by local exposure to foreign antigens. The observation that there is a substantial overlap in the amino acid CDR3 repertoires of the memory CD4⁺ T cells compartment in the two fetuses analyzed may indicate exposure to similar foreign antigens.

Approximately 50% of all fetal intestinal CD4⁺ T cells were CD161⁺ and transcriptionally distinct from their CD161⁻ counterparts, consistent with a recent study³³. The kinetics of *KLRB1* (CD161) expression was preceded by increased expression of CD5 and coincided with increased expression of several TCR signaling genes, including *FYN*, *FASL* and *TNF*, suggesting a coordinated program of transcription. Of note, CD161 was identified as a costimulatory molecule in the context of TCR stimulation³³.

Although the mass cytometry and RNA-seq data were largely compatible, there were exceptions. For example, coexpression of *CCR6* and *KIT* among *KLRB1*⁺*CCR6*⁺*SELL*⁻ T_M cells was not reflected in the gene expression profiles. Conversely, expression of *ITGAE* (CD103) mRNA was not reflected by protein expression. These anomalies were probably attributable to discordant gene transcription and protein expression³⁴ and may also relate to differences in sensitivity of the techniques used.

The presence of a large population of T_N cells in the fetal intestine is in stark contrast to the predominance of T_M cells in the adult intestine. As the T_N cells expressed relatively high amounts of CD31, which demarcates recent thymic emigrants, our results indicate direct migration of recent thymic emigrants into the intestine^{35,36}. We propose that antigen-specific priming of T_N cells takes place in the mesenteric lymph nodes followed by migration of the resulting T_M cells to the lamina propria leading to a progressive loss of T_N cells. Similarly, memory formation is taking place in the CD8⁺ T cell compartment (not shown).

Distinct subpopulations of fetal intestinal T_{reg} cells were distinguished by several markers, including high expression of CD25 and Foxp3, and a lack of CD127. In line with previous results³⁷, approximately 50% of these cells expressed CD45RO, while the remainder expressed CD45RA. The CD45RA⁺ T_{reg} cells expressed TCRs with longer CDR3β loops, higher numbers of added N nucleotides and distinct physicochemical characteristics, suggesting higher affinities for self-antigens compared with CD45RO⁺ T_{reg} cells³⁸. The presence of oligoclonal T cell expansions in fetuses with autoimmune conditions associated with a genetic absence of T_{reg} cells indicate a key role for these cells in immune suppression in utero³⁹.

In conclusion, our study revealed a putative differentiation trajectory in the fetal intestinal CD4⁺ T cell compartment, consistent with the formation of T_M cells in utero, presumably as a consequence of exposure to foreign antigens. These could include non-inherited maternal HLA molecules⁴⁰ and pathogen-derived ligands, which could be derived from amniotic fluid^{8,9}. We propose that immune priming in the fetal intestine prepares the infant for the massive influx of bacteria that occurs immediately after birth, with anamnestic responses in situ facilitated by the colocalization of CD4⁺ T_M cells with APCs.

Online content

Any methods, additional references, Nature Research reporting summaries, source data, statements of data availability and associated accession codes are available at <https://doi.org/10.1038/s41590-018-0294-9>.

Received: 29 May 2018; Accepted: 4 December 2018;
Published online: 21 January 2019

References

- Janeway, C. A. Jr. Approaching the asymptote? Evolution and revolution in immunology. *Cold Spring Harb. Symp. Quant. Biol.* **54**(Pt 1), 1–13 (1989).
- Fan, X. & Rudensky, A. Y. Hallmarks of tissue-resident lymphocytes. *Cell* **164**, 1198–1211 (2016).
- Thome, J. J. C. et al. Early-life compartmentalization of human T cell differentiation and regulatory function in mucosal and lymphoid tissues. *Nat. Med.* **22**, 72–77 (2015).
- Bunders, M. J. et al. Memory CD4(+)CCR5(+) T cells are abundantly present in the gut of newborn infants to facilitate mother-to-child transmission of HIV-1. *Blood* **120**, 4383–4390 (2012).
- Zhang, X. et al. CD4 T cells with effector memory phenotype and function develop in the sterile environment of the fetus. *Sci. Transl. Med.* **6**, 238ra72 (2014).
- Stout, M. J. et al. Identification of intracellular bacteria in the basal plate of the human placenta in term and preterm gestations. *Am. J. Obstet. Gynecol.* **208**, 226.e1–7 (2013).
- Aagaard, K. et al. The placenta harbors a unique microbiome. *Sci. Transl. Med.* **6**, 237ra65 (2014).
- Collado, M. C., Rautava, S., Aakko, J., Isolauri, E. & Salminen, S. Human gut colonisation may be initiated in utero by distinct microbial communities in the placenta and amniotic fluid. *Sci. Rep.* **6**, 23129 (2016).
- DiGiulio, D. B. Diversity of microbes in amniotic fluid. *Semin. Fetal Neonatal Med.* **17**, 2–11 (2012).
- Ardissone, A. N. et al. Meconium microbiome analysis identifies bacteria correlated with premature birth. *PLoS ONE* **9**, e90784 (2014).
- Hornef, M. & Penders, J. Does a prenatal bacterial microbiota exist? *Mucosal Immunol.* **10**, 598–601 (2017).
- Li, N. et al. Mass cytometry reveals innate lymphoid cell differentiation pathways in the human fetal intestine. *J. Exp. Med.* **215**, 1383–1396 (2018).
- van Unen, V. et al. Visual analysis of mass cytometry data by hierarchical stochastic neighbour embedding reveals rare cell types. *Nat. Commun.* **8**, 1740 (2017).
- Maaten, L. vander & Hinton, G. Visualizing data using t-SNE. *J. Mach. Learn. Res.* **9**, 2579–2605 (2008).
- Höltt, T. et al. Cytosplore: interactive immune cell phenotyping for large single-cell datasets. *Comput. Graph. Forum* **35**, 171–180 (2016).
- Butler, A., Hoffman, P., Smibert, P., Papalexi, E. & Satija, R. Integrating single-cell transcriptomic data across different conditions, technologies, and species. *Nat. Biotechnol.* **36**, 411–420 (2018).
- Kimmig, S. et al. Two subsets of naive T helper cells with distinct T cell receptor excision circle content in human adult peripheral blood. *J. Exp. Med.* **195**, 789–794 (2002).
- Angerer, P. et al. destiny: diffusion maps for large-scale single-cell data in R. *Bioinformatics* **32**, 1241–1243 (2015).
- Samusik, N., Good, Z., Spitzer, M. H., Davis, K. L. & Nolan, G. P. Automated mapping of phenotype space with single-cell data. *Nat. Methods* **13**, 493–496 (2016).
- Jolliffe, I. Principal component analysis. in *International Encyclopedia of Statistical Science* (ed. Lovric, M) Ch. 427, 1094–1096 (Springer, Berlin, 2011).
- Trapnell, C. et al. The dynamics and regulators of cell fate decisions are revealed by pseudotemporal ordering of single cells. *Nat. Biotechnol.* **32**, 381–386 (2014).
- Qiu, X. et al. Single-cell mRNA quantification and differential analysis with Census. *Nat. Methods* **14**, 309–315 (2017).
- Azzam, H. S. et al. CD5 expression is developmentally regulated by T cell receptor (TCR) signals and TCR avidity. *J. Exp. Med.* **188**, 2301–2311 (1998).
- Mandl, J. N., Monteiro, J. P., Vriskoop, N. & Germain, R. N. T. Cell-positive selection uses self-ligand binding strength to optimize repertoire recognition of foreign antigens. *Immunity* **38**, 263–274 (2013).
- Persaud, S. P., Parker, C. R., Lo, W.-L., Scott Weber, K. & Allen, P. M. Intrinsic CD4 T cell sensitivity and response to a pathogen are set and sustained by avidity for thymic and peripheral complexes of self peptide and MHC. *Nat. Immunol.* **15**, 266–274 (2014).
- Fulton, R. B. et al. The TCR's sensitivity to self peptide-MHC dictates the ability of naive CD8(+) T cells to respond to foreign antigens. *Nat. Immunol.* **16**, 107–117 (2015).
- Shugay, M. et al. VDJtools: unifying post-analysis of T cell receptor repertoires. *PLoS Comput. Biol.* **11**, e1004503 (2015).
- Egorov, E. S. et al. The changing landscape of naive T cell receptor repertoire with human aging. *Front. Immunol.* **9**, 1618 (2018).
- Miyazawa, S. & Jernigan, R. L. Residue-residue potentials with a favorable contact pair term and an unfavorable high packing density term, for simulation and threading. *J. Mol. Biol.* **256**, 623–644 (1996).

30. Kidera, A., Konishi, Y., Oka, M., Ooi, T. & Scheraga, H. A. Statistical analysis of the physical properties of the 20 naturally occurring amino acids. *J. Protein Chem.* **4**, 23–55 (1985).
31. Rackovsky, S. Global characteristics of protein sequences and their implications. *Proc. Natl Acad. Sci. USA* **107**, 8623–8626 (2010).
32. Pezzotti, N. et al. Approximated and user steerable tSNE for progressive visual analytics. *IEEE Trans. Vis. Comput. Graph.* **23**, 1739–1752 (2017).
33. Fergusson, J. R. et al. CD161 defines a transcriptional and functional phenotype across distinct human T cell lineages. *Cell Rep.* **9**, 1075–1088 (2014).
34. Edfors, F. et al. Gene-specific correlation of RNA and protein levels in human cells and tissues. *Mol. Syst. Biol.* **12**, 883 (2016).
35. McFarland, R. D., Douek, D. C., Koup, R. A. & Picker, L. J. Identification of a human recent thymic emigrant phenotype. *Proc. Natl Acad. Sci. USA* **97**, 4215–4220 (2000).
36. Staton, T. L. et al. CD8⁺ recent thymic emigrants home to and efficiently repopulate the small intestine epithelium. *Nat. Immunol.* **7**, 482–488 (2006).
37. Michaelsson, J., Mold, J. E., McCune, J. M. & Nixon, D. F. Regulation of T cell responses in the developing human fetus. *J. Immunol.* **176**, 5741–5748 (2006).
38. Feng, Y. et al. A mechanism for expansion of regulatory T-cell repertoire and its role in self-tolerance. *Nature* **528**, 132–136 (2015).
39. Allenspach, E. J. et al. Absence of functional fetal regulatory T cells in humans causes in utero organ-specific autoimmunity. *J. Allergy Clin. Immunol.* **140**, 616–619.e7 (2017).
40. Gomez de Agüero, M. et al. The maternal microbiota drives early postnatal innate immune development. *Science* **351**, 1296–1302 (2016).

Acknowledgements

We thank the Center for Contraception, Abortion and Sexuality (Leiden and The Hague) for collection and provision of fetal material, K. Lodder, T. van Herwaarden, M. Bialecka and F. Wang for dissection of fetal tissues, and S. L. Kloet for assistance with single-cell

RNA sequencing. This research was supported by Leiden University Medical Center (N.L., V.v.U., N.G., F.K.), the Netherlands Organization for Scientific Research (NWO Applied Technical Sciences grant no. 12721 and ZonMW grant no. 91112008) (T.A., T.H., J.E., B.P.F.L.), the Russian Science Foundation (grant no. 16-15-00149) (S.A.K., E.S.E., M.I., O.V.B., D.M.C.), the Wellcome Trust (grant no. 100326/Z/12/Z) (K.L., J.E.M., D.A.P.), the European Commission under an MSCA-ITN award (grant no. 675743/ISPIC) (T.A.), and the China Scholarship Council (N.L. and N.G.).

Author contributions

N.L., V.v.U. and F.K. conceived the study and wrote the manuscript. N.L. performed most of the experiments with help from V.v.U. and N.G. N.L. performed most of the data analyses with help from V.v.U., T.A. and B.P.F.L. S.A.K., K.L., J.E.M., E.S.E., M.I., D.M.C., O.V.B. and D.A.P. performed TCR repertoire analyses. D.A.P. revised the manuscript. N.F.C.d.M. helped with imaging mass cytometry experiments. T.H., V.v.U., J.E. and B.P.F.L. developed Cytosplore. S.M.C.d.S.L. provided human fetal tissues. All authors discussed the results and helped prepare the final manuscript.

Competing interests

The authors declare no competing interests.

Additional information

Supplementary information is available for this paper at <https://doi.org/10.1038/s41590-018-0294-9>.

Reprints and permissions information is available at www.nature.com/reprints.

Correspondence and requests for materials should be addressed to F.K.

Publisher's note: Springer Nature remains neutral with regard to jurisdictional claims in published maps and institutional affiliations.

© The Author(s), under exclusive licence to Springer Nature America, Inc. 2019

Methods

Sample processing and cell isolation. Fetal tissues were obtained from elective abortions with informed consent. The gestational age ranged from 14 to 22 weeks. Intestines were separated from mesentery, cut into small pieces, embedded in optimal cutting temperature compound and snap-frozen in isopentane. The remaining intestines were used for single-cell isolation as described previously¹². Briefly, fetal intestines were cleared of meconium, cut into fine pieces, treated with 1 mM dithiothreitol (Fluka) for 2 × 10 min (replacing buffer) at room temperature, and then incubated with 1 mM ethylenediaminetetraacetic acid (Merck) for 2 × 1 h (replacing buffer) at 37 °C under rotation to separate the epithelium from the lamina propria. To obtain single-cell suspensions from the lamina propria, the intestines were rinsed with Hank's balanced salt solution (ThermoFisher Scientific), incubated with 10 U ml⁻¹ collagenase IV (Worthington) and 200 μg ml⁻¹ DNase I grade II (Roche Diagnostics) overnight at 37 °C, and filtered through a 70 μm nylon mesh. Isolated cells were then further purified with a Percoll gradient (GE Healthcare). Fetal liver and spleen tissues were cut into small pieces and filtered through a 70 μm nylon cell strainer and the immune cells were isolated with Ficol-Paque density gradient (provided by the pharmacy of Leiden University Medical Center). All the isolated cells were stored in liquid nitrogen. Study approval was granted by the Medical Ethics Commission of Leiden University Medical Centre (protocol P08.087). All experiments were conducted in accordance with local ethical guidelines and the principles of the Declaration of Helsinki.

Cell suspension mass cytometry. Antibodies used for cell suspension mass cytometry are listed in Supplementary Table 1. Purified antibodies lacking carrier protein were conjugated with metal reporters by using a MaxPar X8 Antibody Labeling Kit (Fluidigm). Procedures for antibody staining and data acquisition were described previously⁴¹. Briefly, cells from fetal intestines were incubated with 5 μM Cell-ID Intercalator-¹⁰⁹Rh (Fluidigm) for 15 min at room temperature and then stained with a cocktail of metal-conjugated antibodies for 45 min at room temperature. After washing, cells were incubated with 125 nM Cell-ID Intercalator-Ir (Fluidigm) in MaxPar Fix and Perm Buffer (Fluidigm) overnight at 4 °C. Data were acquired using a CyTOF 2 mass cytometer (Fluidigm) and normalized using EQ Four Element Calibration Beads with the reference EQ Passport P13H2302 (Fluidigm).

Imaging mass cytometry. Antibodies used for imaging mass cytometry are listed in Supplementary Table 3. Purified antibodies lacking carrier protein were conjugated with metal reporters by using a MaxPar X8 Antibody Labeling Kit (Fluidigm). Snap-frozen human fetal intestinal biopsies were sectioned at a thickness of 5 μm and fixed by incubating with 1% paraformaldehyde for 5 min at room temperature followed by 100% methanol for 5 min at -20 °C. After fixation, tissue sections were washed in Dulbecco's phosphate-buffered saline (ThermoFisher Scientific) containing 0.5% bovine serum albumin and 0.05% Tween, rehydrated in additive-free Dulbecco's phosphate-buffered saline, washed again and blocked with Superblock Solution (ThermoFisher Scientific). Tissue sections were then stained with a cocktail of metal-conjugated antibodies overnight at 4 °C, washed and incubated with 125 nM Cell-ID Intercalator-Ir for 30 min at room temperature. After a further wash, tissue sections were dipped in Milli-Q water (Merck Millipore) for 1 min and dried for 20 min at room temperature. Data were acquired using a Hyperion imaging mass cytometer (Fluidigm) at a resolution of 1 μm, with settings aligned to company guidelines. The ablation frequency was 200 Hz, and the energy was 6 dB. Regions of interest were acquired at a size of 1 × 1 mm². All data were stored as MCD files and txt files.

Single-cell RNA sequencing. Single, live, CD8α⁺TCRγδ⁺CD4⁺ cells from the intestines of fetus no. 6 were sorted using a FACSAria III flow cytometer (BD Biosciences). Post-sort purity was 96.5%. Single-cell RNA sequencing was performed as described previously⁴². Briefly, cells combined with oil, reagents and beads were loaded on a Chromium Single Cell Controller (10x Genomics). Lysis and barcoded reverse transcription of polyadenylated mRNA from single cells were performed inside each gel bead emulsion. Next-generation sequencing libraries were prepared in a single bulk reaction, and transcripts were sequenced using a HiSeq4000 System (Illumina).

Integrated data analysis. For cell suspension mass cytometry, data from single, live, CD45⁺ cells, gated individually using Cytobank as shown in Supplementary Fig. 1a, were sample-tagged and hyperbolic-arc-sinh-transformed with a cofactor of 5 using Cytosplore^{HSNE} software¹³. The major immune lineages shown in Supplementary Fig. 1b were then identified at the overview level by performing a three-level HSNE analysis carried out with default parameters (perplexity: 30; iterations: 1,000). All t-SNE plots and Gaussian mean-shift clustering-derived cell clusters were generated in Cytosplore¹⁵. Hierarchical clustering of the phenotype heat map was created with Euclidean correction and average linkage clustering in Cytosplore^{HSNE}. Violin plots for cytometry data were generated in R. Diffusion map plots for mass cytometry data were generated using the 'density' package in R. Single-cell force-directed layouts for mass cytometry data were generated using Vortex software¹⁹. For imaging mass cytometry, all images were generated using

MCD Viewer software v1.0.560 (Fluidigm). For single-cell RNA-seq, single-cell transcriptome sequencing data were processed using the single-cell RNA-seq package Seurat in R¹⁶. The Seurat object was generated by following the criteria that each gene was expressed by at least three cells and that at least 200 genes were expressed per cell. Data were further filtered on the basis of the parameters: (1) unique gene count per cell >200 and <2,000; and (2) mitochondrial percentage of all genes <0.05. After log-normalization, a PCA-reduction analysis (pca.compute = 20) was performed on the basis of the 2,174 variable genes across single cells. Next, graph-based clustering detection and a t-SNE algorithm were applied to the top 13 PCA dimensions. The resolution for cluster detection was 0.8. Heat maps, PCA plots, diffusion map plots and violin plots of the RNA-seq data were generated using the Seurat package. The t-SNE plots for RNA-seq data shown in Fig. 4b were generated in Cytosplore^{HSNE}. Only genes with local standardization (>0.5) across all cells were taken into account. Bar graphs and dot plots (showing mean and s.d.) were generated in Prism (GraphPad). The pseudotime analysis shown in Fig. 4c,d was performed using the Monocle 2 toolkit in R as described previously²², excluding unrelated T_{reg} cells. Briefly, the single-cell trajectory was inferred using the dpFeature unsupervised procedure to identify variable genes, and the dimensions were reduced using t-SNE on the top high-loading principal components. The top 1,000 significant genes were selected as the ordering genes and reduced with the DDRTree method for the single-cell graph shown in Fig. 4c. Variable genes were selected at a significant false discovery rate of <10%, clustered by pseudotemporal expression patterns, and visualized in a heat map in Fig. 4d. We performed gene list enrichment analysis using ToppGene⁴³, gene interaction network analysis using the BioGrid interaction database⁴⁴ and gene pathway analysis using the Kyoto Encyclopedia of Genes and Genomes⁴⁵.

Flow cytometry. For surface staining, cells were incubated with fluorochrome-conjugated antibodies and human Fc block (BioLegend) for 30–45 min at 4 °C. For intracellular cytokine/CD154 staining, cells were stimulated with CD3/CD28-specific (2.5 μg ml⁻¹ each, BioLegend) or control antibodies (5 μg ml⁻¹, BioLegend) for 4 h at 37 °C. Brefeldin A (10 μg ml⁻¹, Sigma) was added for the final 3 h. Cells were then fixed/permeabilized using Fixation Buffer and Intracellular Staining Perm Wash Buffer (BioLegend). For intracellular Foxp3/Ki-67 staining, cells were prepared using a Foxp3 Staining Buffer Set (eBioscience). Electronic compensation was performed using individually stained CompBeads (BD Biosciences). Cells were acquired using an LSR II cytometer (BD Biosciences) or sorted using a FACSAria III flow cytometer (BD Biosciences) as shown in Supplementary Fig. 3a. Data were analyzed with FlowJo software v10 (Tree Star Inc.). The antibodies used in this study are listed in Supplementary Table 4.

TCR repertoire analysis. CD4⁺ T cell subsets were sorted according to the gating strategy shown in Supplementary Fig. 3a. For conventional sequencing, a total of 5,000 cells per subset was sorted directly into RNAlater (Applied Biosystems) using a FACSAria III flow cytometer (BD Biosciences). All expressed TCRβ rearrangements were amplified using a template-switch anchored RT-PCR, sequenced and analyzed as described previously⁴⁶. Gene use was determined according to the ImMunoGeneTics nomenclature⁴⁷.

For high-throughput sequencing, an average of 6,700 ± 2,000 cells per subset was sorted directly into RLT buffer (Qiagen) using a FACSAria III flow cytometer (BD Biosciences). Four volumes of TRIzol (Invitrogen) were then added to the RLT cell lysate. RNA was extracted according to the TRIzol Reagent User Guide. Unique molecular identifier-labeled 5' RACE TCRα and TCRβ complementary DNA libraries were prepared using a Human TCR Profiling Kit (MiLaboratory LLC). All extracted RNA was used for cDNA synthesis, and all synthesized cDNA was used for PCR amplification. Libraries were prepared in parallel using the same number of PCR cycles and sequenced in parallel using a 150 + 150 base pair MiSeq System (Illumina). This approach generated a total of 11,310,000 TCRα and TCRβ sequencing reads (250,000 ± 150,000 reads per library), from which 625,000 unique molecular identifier-labeled TCR cDNA molecules (13,500 ± 7,000 molecules per library) were extracted using MIGEC⁴⁸ and MiXCR⁴⁹ software with a threshold of at least two sequencing reads per unique molecular identifier. Each library contained an average of 3,500 ± 1,300 functional (in-frame, without stop codons) CDR3 nucleotide sequences. Averaged TCR repertoire characteristics weighted by clonotype size were analyzed using VDJtools software²⁷. Gene use was determined according to the ImMunoGeneTics nomenclature⁴⁷.

Statistics. Results are shown as mean ± s.e.m. The statistics tests used were two-tailed Wilcoxon matched-pairs signed-ranks test and Kruskal–Wallis test with Dunn's test for multiple group comparisons, as appropriate (after normality test). $P \leq 0.05$ was considered to be statistically significant. All statistics were analyzed using GraphPad Prism7 software.

Reporting Summary. Further information on research design is available in the Nature Research Reporting Summary linked to this article.

Data availability

Mass cytometry data are available via Flow Repository (<https://flowrepository.org/id/FR-FCM-ZYRD>). Single-cell RNA-seq data are available via Gene Expression

Omnibus accession code [GSE122846](#). The remaining data that support the findings of this study are available from the corresponding author upon reasonable request.

References

41. van Unen, V. et al. Mass cytometry of the human mucosal immune system identifies tissue- and disease-associated immune subsets. *Immunity* **44**, 1227–1239 (2016).
42. Zheng, G. X. Y. et al. Massively parallel digital transcriptional profiling of single cells. *Nat. Commun.* **8**, 14049 (2017).
43. Chen, J., Bardes, E. E., Aronow, B. J. & Jegga, A. G. ToppGene Suite for gene list enrichment analysis and candidate gene prioritization. *Nucleic Acids Res.* **37**, W305–W311 (2009).
44. Bean, D. M. et al. esyN: network building, sharing and publishing. *PLoS ONE* **9**, e106035 (2014).
45. Ogata, H. et al. KEGG: Kyoto Encyclopedia of Genes and Genomes. *Nucleic Acids Res.* **27**, 29–34 (1999).
46. Quigley, M. F., Almeida, J. R., Price, D. A. & Douek, D. C. Unbiased molecular analysis of T cell receptor expression using template-switch anchored RT-PCR. *Curr. Protoc. Immunol.* **94**, 10.33.1–10.33.16 (2011).
47. Lefranc, M.-P. et al. IMGT unique numbering for immunoglobulin and T cell receptor constant domains and Ig superfamily C-like domains. *Dev. Comp. Immunol.* **29**, 185–203 (2005).
48. Shugay, M. et al. Towards error-free profiling of immune repertoires. *Nat. Methods* **11**, 653–655 (2014).
49. Bolotin, D. A. et al. MiXCR: software for comprehensive adaptive immunity profiling. *Nat. Methods* **12**, 380–381 (2015).

Reporting Summary

Nature Research wishes to improve the reproducibility of the work that we publish. This form provides structure for consistency and transparency in reporting. For further information on Nature Research policies, see [Authors & Referees](#) and the [Editorial Policy Checklist](#).

Statistical parameters

When statistical analyses are reported, confirm that the following items are present in the relevant location (e.g. figure legend, table legend, main text, or Methods section).

n/a Confirmed

- The exact sample size (n) for each experimental group/condition, given as a discrete number and unit of measurement
- An indication of whether measurements were taken from distinct samples or whether the same sample was measured repeatedly
- The statistical test(s) used AND whether they are one- or two-sided
Only common tests should be described solely by name; describe more complex techniques in the Methods section.
- A description of all covariates tested
- A description of any assumptions or corrections, such as tests of normality and adjustment for multiple comparisons
- A full description of the statistics including central tendency (e.g. means) or other basic estimates (e.g. regression coefficient) AND variation (e.g. standard deviation) or associated estimates of uncertainty (e.g. confidence intervals)
- For null hypothesis testing, the test statistic (e.g. F , t , r) with confidence intervals, effect sizes, degrees of freedom and P value noted
Give P values as exact values whenever suitable.
- For Bayesian analysis, information on the choice of priors and Markov chain Monte Carlo settings
- For hierarchical and complex designs, identification of the appropriate level for tests and full reporting of outcomes
- Estimates of effect sizes (e.g. Cohen's d , Pearson's r), indicating how they were calculated
- Clearly defined error bars
State explicitly what error bars represent (e.g. SD , SE , CI)

Our web collection on [statistics for biologists](#) may be useful.

Software and code

Policy information about [availability of computer code](#)

Data collection

Data for suspension-mass cytometry were acquired using a CyTOF 2 mass cytometer (Fluidigm). Data for imaging-mass cytometry were acquired using a Hyperion imaging-mass cytometer (Fluidigm) at 1 μm resolution with the settings aligned to company guidelines. Data for RNA-seq were collected using an Illumina HiSeq4000 (10x Genomics). Data for flow cytometry were acquired using an LSR II cytometer (BD Biosciences). Data for bulk TCR repertoire analysis were generated using a template-switch anchored RT-PCR. Data for deep TCR- α and - β sequencing were acquired using Illumina MiSeq.

Data analysis

Cytosplore, Cytobank, Vortex and "density" package in R 3.4.1 were used for mass cytometry analysis. RNA-seq data were analyzed using "Seurat" and "Monocle 2" packages in R 3.4.1 and Cytosplore. Gene list enrichment analysis was performed using ToppGene, gene interaction network analysis was performed using the BioGrid interaction database and gene pathway analysis was performed using the Kyoto Encyclopedia of Genes and Genomes (KEGG). Data for deep TCR- α and - β sequencing were analyzed using VDJtools software. TCR- α and - β sequencing reads were extracted using MIGEC49 and MiXCR50 software with a threshold of at least 2 sequencing reads per UMI. For imaging-mass cytometry, all images were generated using MCD Viewer software v1.0.560 (Fluidigm). Flow cytometry data were analyzed with FlowJo v10 software (Tree Star Inc.). Bar graphs and dot plots (showing mean and SEM or SD) were generated in Graphpad Prism 7. All the statistics were also generated in Graphpad Prism 7.

For manuscripts utilizing custom algorithms or software that are central to the research but not yet described in published literature, software must be made available to editors/reviewers upon request. We strongly encourage code deposition in a community repository (e.g. GitHub). See the Nature Research [guidelines for submitting code & software](#) for further information.

Data

Policy information about [availability of data](#)

All manuscripts must include a [data availability statement](#). This statement should provide the following information, where applicable:

- Accession codes, unique identifiers, or web links for publicly available datasets
- A list of figures that have associated raw data
- A description of any restrictions on data availability

Mass cytometry data are available via Flow Repository (<https://flowrepository.org/id/FR-FCM-ZYRD>). scRNA-seq data are available via Gene Expression Omnibus accession code GSE122846. The remaining data that support the findings of this study are available from the corresponding author upon reasonable request.

Field-specific reporting

Please select the best fit for your research. If you are not sure, read the appropriate sections before making your selection.

Life sciences Behavioural & social sciences Ecological, evolutionary & environmental sciences

For a reference copy of the document with all sections, see [nature.com/authors/policies/ReportingSummary-flat.pdf](https://www.nature.com/authors/policies/ReportingSummary-flat.pdf)

Life sciences study design

All studies must disclose on these points even when the disclosure is negative.

Sample size	In this study no statistical methods were used to predetermine sample size and a total of ~70 unique human fetal intestines were used. For the high-dimensional single-cell assays the number was chosen to obtain sufficient number of immune cells to capture the heterogeneity. High-dimensional single-cell data revealed that a highly similar composition of the CD4+ T cell compartment in all samples, despite quantitative differences. For the functional studies, replicates were included to reproduce findings in independent experiments. All replication attempts were successful. See Figure legends for these specifications. In addition, 3 fetal livers and 3 fetal spleens were used for mass cytometry analysis to compare the immune composition among tissues.
Data exclusions	In accordance with current practice in the field, single cells which failed standard QC for RNA-seq were excluded from analysis. The exclusion criteria were described in the Method Section.
Replication	All attempts at replication were successful.
Randomization	All experiments were performed using randomly selected human fetal intestines, livers and spleens.
Blinding	No blinding test in this study. Since all the samples were selected and grouped randomly and data collection and /or analysis were mainly performed using computational tool, we consider that blinding was not applicable to the current study.

Reporting for specific materials, systems and methods

Materials & experimental systems

n/a	Involved in the study
<input checked="" type="checkbox"/>	<input type="checkbox"/> Unique biological materials
<input type="checkbox"/>	<input checked="" type="checkbox"/> Antibodies
<input checked="" type="checkbox"/>	<input type="checkbox"/> Eukaryotic cell lines
<input checked="" type="checkbox"/>	<input type="checkbox"/> Palaeontology
<input checked="" type="checkbox"/>	<input type="checkbox"/> Animals and other organisms
<input type="checkbox"/>	<input checked="" type="checkbox"/> Human research participants

Methods

n/a	Involved in the study
<input checked="" type="checkbox"/>	<input type="checkbox"/> ChIP-seq
<input type="checkbox"/>	<input checked="" type="checkbox"/> Flow cytometry
<input checked="" type="checkbox"/>	<input type="checkbox"/> MRI-based neuroimaging

Antibodies

Antibodies used

Antibodies were purchased from indicated company. For mass cytometry, purified antibodies lacking carrier protein were conjugated with metal reporters by using a MaxPar X8 Antibody Labeling Kit (Fluidigm).
 CyTOF antibodies:
 Antigen Tag Clone Supplier Cat. Final dilution
 1 CD127 165Ho AO19D5 Flui 3165008B 1/800
 2 CCR6 141Pr G034E3 Flui 3141003A 1/200

3 CD8a 146Nd RPA-T8 Flui 3146001B 1/200
 4 CD11c 162Dy Bu15 Flui 3162005B 1/200
 5 CD38 172Yb HIT2 Flui 3172007B 1/200
 6 CD45 89Y HI30 Flui 3089003B 1/100
 7 CD117 143Nd 104D2 Flui 3143001B 1/100
 8 CD4 145Nd RPA-T4 Flui 3145001B 1/100
 9 CD16 148Nd 3G8 Flui 3148004B 1/100
 10 CD25 149Sm 2A3 Flui 3149010B 1/100
 11 CD123 151Eu 6H6 Flui 3151001B 1/100
 12 CD7 153Eu CD7-6B7 Flui 3153014B 1/100
 13 CD163 154Sm GHI/61 Flui 3154007B 1/100
 14 CCR7 159Tb G043H7 Flui 3159003A 1/100
 15 CD14 160Gd M5E2 Flui 3160001B 1/100
 16 CD161 164Dy HP-3G10 Flui 3164009B 1/100
 17 CD27 167Er O323 Flui 3167002B 1/100
 18 CD45RA 169Tm HI100 Flui 3169008B 1/100
 19 CD3 170Er UCHT1 Flui 3170001B 1/100
 20 PD-1 175Lu EH 12.2H7 Flui 3175008B 1/100
 21 CD56 176Yb NCAM16.2 Flui 3176008B 1/100
 22 CD11b 144Nd ICRF44 Flui 3144001B 1/100
 23 TCR $\gamma\delta$ 152Sm 11F2 Flui 3152008B 1/50
 24 HLA-DR 168Er L243 BioL 307651 1/200
 25 CD20 163Dy 2H7 BioL 302343 1/200
 26 CD34 142Nd HIB19 BioL 343531 1/100
 27 IgM 150Nd MHM88 BioL 314527 1/100
 28 CD103 155Gd Ber-ACT8 BioL 350202 1/100
 29 CRTH2 156Gd BM16 BioL 350102 1/100
 30 CD28 171Yb CD28.2 BioL 302902 1/100
 31 CD45RO 173Yb UCHL1 BioL 304239 1/100
 32 CD122 158Gd TU27 BioL 339002 1/50
 33 KLRG-1 161Dy REA261 MACS 120-014-229 1/50
 34 CD8b 166Er SIDI8BEE eBio 14-5273 1/50
 35 NKp46 174Yb 9E2 BioL 331902 1/40
 Fluidigm (Flui), eBioscience (eBio) and Biolegend (BioL).

Imaging-mass cytometry antibody panel:

Antigen Tag Clone Supplier Cat. Final dilution

1 CD45 89Y HI30 Flui 3089003B 1/50
 2 CD3 170Er UCHT1 Flui 3170001B 1/100
 3 CD7 153Eu CD7-6B7 Flui 3153014B 1/100
 4 CD4 145Nd RPA-T4 Flui 3145001B 1/50
 5 CD38 172Yb HIT2 Flui 3172007B 1/50
 6 CD8a 146Nd RPA-T8 Flui 3146001B 1/50
 7 CD45RA 169Tm HI100 Flui 3169008B 1/100
 8 Ki-67 166Er D3B5 CST CST9129BF 1/200
 9 CD161 164Dy HP-3G10 Flui 3164009B 1/50
 10 CD69 144Nd FN50 Flui 3149010B 1/50
 11 CD163 154Sm GHI/61 Flui 3154007B 1/100
 12 HLA-DR 168Er L243 BioL 307651 1/300
 13 Collagen I 147Sm polyclonal Millipore AB758 1/100
 14 Vimentin 175Lu D21H3 CST CST5741BF 1/200
 15 SMA 148Nd 1A4 CST CST5685BF 1/200
 16 E-Cadherin 150Nd 2.40E+11 CST CST3195BF 1/50
 Fluidigm (Flui), Cell Signaling Technology (CST) and Biolegend (BioL)

Antigen clone Flourchrome Supplier Final dilution

1 CD3 SK7 Amcyan BD 1/25
 2 CD4 RPA-T4 BV421 BioL 1/100
 3 CD5 L17F12 PE BD 1/200
 4 CD8a RPA-T8 BV650 BD 1/200
 5 TCR $\gamma\delta$ 11F2 BV650 BD 1/40
 6 CD25 M-A251 PE-cy7 BD 1/100
 7 CD31 WM59 PE BD 1/20
 8 CD45RO UCHL1 PerCP/Cy5.5 BioL 1/20
 9 CD45RA HI100 PE/Dazzle BioL 1/20
 10 CD62L SK11 PE BD 1/10
 11 CD69 FN50 PE BD 1/20
 12 CD127 A019D5 PE BioL 1/80
 13 CD127 A019D5 FITC BioL 1/20
 14 CD127 A019D5 PE-cy7 BioL 1/150
 15 CD117 YB5.B8 APC BD 1/20
 16 CD154 24-31 BV605 BioL 1/20
 17 CD161 DX12 BV605 BD 1/20
 18 CXCR3 1C6 PE BD 1/30
 19 CCR4 1G1 PE BD 1/10

20 DNAM-1 DX11 PE BD 1/10
 21 TNF MAb11 PE-cy7 eBio 1/500
 22 IFN- γ 4S.B3 PE BioL 1/20
 23 IFN- γ 4S.B3 BV421 BioL 1/10
 24 IL-4 MP4-25D2 FITC BD 1/50
 25 IL-17A BL168 BV421 BioL 1/20
 26 IL-2 MQ1-17H12 BV650 BioL 1/40
 27 Ki-67 20Raj1 FITC eBio 1/20
 28 Ki-67 20Raj1 PE eBio 1/50
 29 Granzyme B GB11 PE eBio 1/50
 30 Foxp3 PCH101 PE eBio 1/20
 eBioscience (eBio), and Biolegend (BioL).

Validation

All antibodies were verified by staining human peripheral blood mononuclear cell and/or cell lines with known expression or not. The data for validation cell-suspension mass cytometry panel have been provided in our previous study.(DOI: 10.1084/jem.20171934)

Human research participants

Policy information about [studies involving human research participants](#)

Population characteristics

Fetal tissues were obtained from elective abortions with informed consent. The gestational age ranged from 14 to 22 weeks. The gender were mixed.

Recruitment

The patients who did elective abortions in the Contraception, Abortion and Sexuality (CASA) in Leiden and The Hague were included after informed consent. The gestational age of the fetuses ranged from 14 to 22 weeks. The gender were mixed.

Flow Cytometry

Plots

Confirm that:

- The axis labels state the marker and fluorochrome used (e.g. CD4-FITC).
- The axis scales are clearly visible. Include numbers along axes only for bottom left plot of group (a 'group' is an analysis of identical markers).
- All plots are contour plots with outliers or pseudocolor plots.
- A numerical value for number of cells or percentage (with statistics) is provided.

Methodology

Sample preparation

All the immune cells were isolated from human fetal intestines and stored in liquid nitrogen. Before staining, the cells were thawed and stained as described in Methods.

Instrument

LSR II cytometer (for acquisition, BD Biosciences); FACSAria III (for sorting, BD Biosciences)

Software

FACS Diva (version 8 or greater) was used for data acquisition. Flow cytometry data were analyzed with FlowJo v10 software (Tree Star Inc.) and R 3.4.1 .

Cell population abundance

All cell populations were distinct and purity was 95%-99%.

Gating strategy

All acquired cells were first gated on FCS/SSC and FCS/FCH to obtained the single live cells. Based on the unstained sample and Full-Minus-One controls to set the positive and negative gates. Every Flow cytometry experiment, a peripheral blood mononuclear cell control sample was included as staining and gating control. The gating strategy for the CD4+ T cell clusters has been shown in Supplementary Figure 3a.

- Tick this box to confirm that a figure exemplifying the gating strategy is provided in the Supplementary Information.